Periodic Buckling of Soft 3D Printed Bioinspired Tubes

Jiayu Liu[a], Wangqu Liu[b], Aishwarya Pantula[b], Zheliang Wang[a], David H. Gracias[b,c], Thao D. Nguyen[a,c,*]

[a]*Department of Mechanical Engineering, The Johns Hopkins University, Baltimore, MD 21218, USA*
[b]*Department of Chemical and Biomolecular Engineering, The Johns Hopkins University, Baltimore, MD 21218, USA*
[c]*Department of Materials Science and Engineering, The Johns Hopkins University, Baltimore, MD 21218, USA*

Abstract

Buckled surfaces induced by mismatched swelling and elastic properties of materials are commonly observed in nature, such as on cacti and euphorbias. The rational design and mimicry of such buckling surfaces could lead to the development of smart, adaptive, and stimuli responsive devices. We designed a 3D printed tubular structure, composed of soft swellable poly N-isopropylacrylamide (pNIPAM) segments and stiff non-swellable poly acrylamide (pAAM) segments. Similar to the shape change of Saguaro stems after rainfall, the tubes show tunable periodic buckling modes in water at the room temperature. The buckling behavior was harnessed through the development of compressive stresses in the soft swellable segments induced by the constraint of the stiff non-swellable segments. We developed a finite element model to explore the design space of this periodic buckling behavior for the tube, and used a chemo-mechanically coupled constitutive model to describe the swellable hydrogel. Inspired by the classic bar buckling problem, we constructed a phase diagram and discovered a universal design parameter that combines the effects of geometric and material properties to guide the design of periodic buckling tubes for bioinspired functional gel structures.

Keywords: 4D printing, Buckling modes, Finite element simulation, Soft robotics

1. Introduction

Cacti and euphorbias are two families of plants that grow in the arid desert environments of North America and Africa, respectively. To survive the harsh arid environment, many of these plants have evolved stems with longitudinal ribs that can shrink and expand like an accordion. The ribs contract during periods of dry hot weather, which shades large areas of the plant and reduces water loss [1, 2]. The ribs also serve to increase the mechanical stability of the plants during rapid expansion. The plants imbibe a large volume of water after a heavy rain fall, which increases the weight and compressive loading on the stems. The expanding ribs allows the large volume increase to be accommodated through a large expansion of the cross-sectional area rather than elongation. This decreases the slenderness ratio of the stems and increases the stability against buckling [3]. As cacti grow, the stems become taller and more slender

*Corresponding author
Email address: vicky.nguyen@jhu.edu (Thao D. Nguyen)

[3], and develop more longitudinal ribs. Saguaro cacti usually have 6-20 ribs and the number of ribs is proportional to the height of the stem to provide mechanical support and improve the stability of the plants [4].

Inspired by the anisotropic periodic swelling of the ribbed stems, we designed 4D printed hydrogel tubes with alternating vertical segments of a thermoresponsive swelling poly *N*-isopropylacrylamide (pNIPAM) gel, representing the longitudinal ribs, and a passive polyacrylamide (pAAM) gel [5]. The thermoresponsive pNIPAM experiences a lower critical solution temperature (LCST) transition that causes it to transform from a hydrophilic to hydrophobic material when heated above the LCST and deswell [6]. The transformation is reversed by cooling to below the LCST allowing the material to swell. We found that the swelling of the vertical pNIPAM segments constrained on both sides by the nonswelling gel segments caused the tube to buckle and develop periodic circumferential folds. The axisymmetric buckling mode allows the tube to accommodate the large volume increase by area expansion with little axial elongation, in a manner similar to the longitudinal ribs in the stem of cacti and euphorbia plants. The circumferential folds can also be found on cacti with long columnar stems, such as the saguaro (Fig. 1a), and may have developed from the axisymmetric buckling of the stems after a large water uptake.

The aim of this work was to investigate the axisymmetric periodic buckling of 4D printed hydrogel tubes with alternating vertical segments of soft swelling and stiff non-swelling hydrogels using a combined theoretical and computational approach. The role of mechanics in the pattern formation and function of plants is widely accepted [7] and many investigators have applied beam, plate, and shell buckling theories to explain the shape and surface patterns on plant structures. Liu et al. [8] applied a chemo-mechanical model for the coupled swelling and elastic deformation of hydrogels in finite element simulations to show how the growth and drying of a thin surface layer on a thick substrate can induce the buckling formation of regularly spaced longitudinal ridges and wrinkle patterns found in a wide array of squashes, bitter gourd and fruits. Chen et al. [9, 10] established a quantitative mechanics framework for stress-driven buckling of spheroidal thin film/substrate system to explore the morphologies of biological systems and the possibilities of manipulating the undulations. Shipman et al. and Steele et al. [11, 12, 13, 14, 15] used the energy-minimizing buckling patterns of a compressed shell on an elastic foundation to study the formation of phyllotaxis, the patterns seen in plants shoots and flowers. Amar et al. [16, 17] adopted Föppl-von Kármán theory to investigate the growth-induced morphogenesis of plants. Mahadevan et al. [18, 19, 20] used a combination of mathematical model, stability analysis and numerical simulation to examine a variety of plant growth processes, including the snap buckling of Venus flytrap, the deformation of long leaf, and the origin of tendril coiling. Yang et al. [21] studied a soft shell sliding on a rigid cylinder and revealed the smooth-wrinkle-ridge-sagging pattern transitions of rolling up a sleeve. Holmes et al. [22] investigated the periodic buckling patterns of elastic shells when subjected to different geometric confinement and found a geometric parameter to predict the number of lobes formed. In this study, we applied finite element analysis that used a chemo-mechanical model for hydrogels, to evaluate the effect of geometry and material properties of the swelling and non-swelling vertical segments on the periodic buckling mode. We next analyzed the buckling of a bar on an elastic foundation to develop a design parameter for the buckling mode of the tube. The design parameter combines

the effects of geometry of the tube and material properties of segments to predict the periodic buckling modes and the associated number of buckles. We applied the design parameter to construct a phase diagram to guide the design and application of the anisotropic swelling properties of periodic buckling of the hydrogel tubes. We observed good agreement between simulations and experiments and uncovered a buckling parameter that can be used to predict the number of buckles. Our studies provide a framework for rational design of tubular mechanical structures of relevance to biomedical implants and soft robotics [23].

2. Method

2.1. Material synthesis and 4D printing

The self-morphing accordion structures were fabricated using 4D printing process described in detail in a prior publication [5] (Fig: 1d). First, active NIPAM ink and passive AAM ink with shear-thinning properties were prepared by mixing shear-thinning agent (Laponite nanoclay), photo-initiator, chemical crosslinker, corresponding monomers and fluorescent dyes using magnetic stirring followed by planetary mixing (Mazerustar KK-250S, Kurabo Industry). The inks were transferred to UV-shielded cartridges and centrifuged to remove air bubbles. The inks were kept at room temperature for at least 24 hrs to allow thorough hydration needed for the desired shear thinning properties. The cartridges were attached to the dual-nozzle Direct Ink Writing 3D Printer (Inkredible+ 3D Bioprinter, Cellink) and connected to an air pump pressure control. Printing nozzles 22G (diameter 0.41 mm) were used to ensure smooth and clog-free printing. The computer-aided-design (CAD) and STL files were created in SolidWorks (Dassault Systèmes), and the G-code files were generated using an independent software project Slic3r (http://slic3r.org/) with layer height 0.4 mm and printing speed 10 mm/s to control the movement of printing nozzles. Before printing, the two printing nozzles were carefully calibrated in x, y, and z directions to ensure seamless switching of two materials. This is essential for printing tall 3D structures because small recurring misalignments over 50-100 printing layers result in significant defects in the final structure. The structures were printed on silicon wafers at room temperature in air at a speed of 10 mm/s. The pressures used for printing the active and passive inks were 90-100 kPa and 110-130 kPa, respectively. After printing, the tubular pregel structures were crosslinked by photocuring using a rotating platform (9.6 rpm) and an Omnicure UV source (LX500, Lumen Dynamics) to enable uniform exposure of UV light and crosslinking. Two UV LED heads (365 nm wavelength) were used to cure the tubular structures with intensity of 0.4 W/cm^2. The tubular structures were photocured section by section and exposure time of nine minutes on each section.

For the actuation experiments, the photocured tubular structures were immersed in deionized (DI) water at room temperature. The structures were allowed to swell for at least 24 hrs to reach a swollen equilibrium state. All optical images were taken in a dark room with a digital camera (EOS 70D, Canon) and a broad spectrum UV light source (EF-160C, Spectronics) to excite the fluorescent dyes in the inks. The photographs of the photocured tubes were taken in the air and those of the transformed structures were taken in DI water.

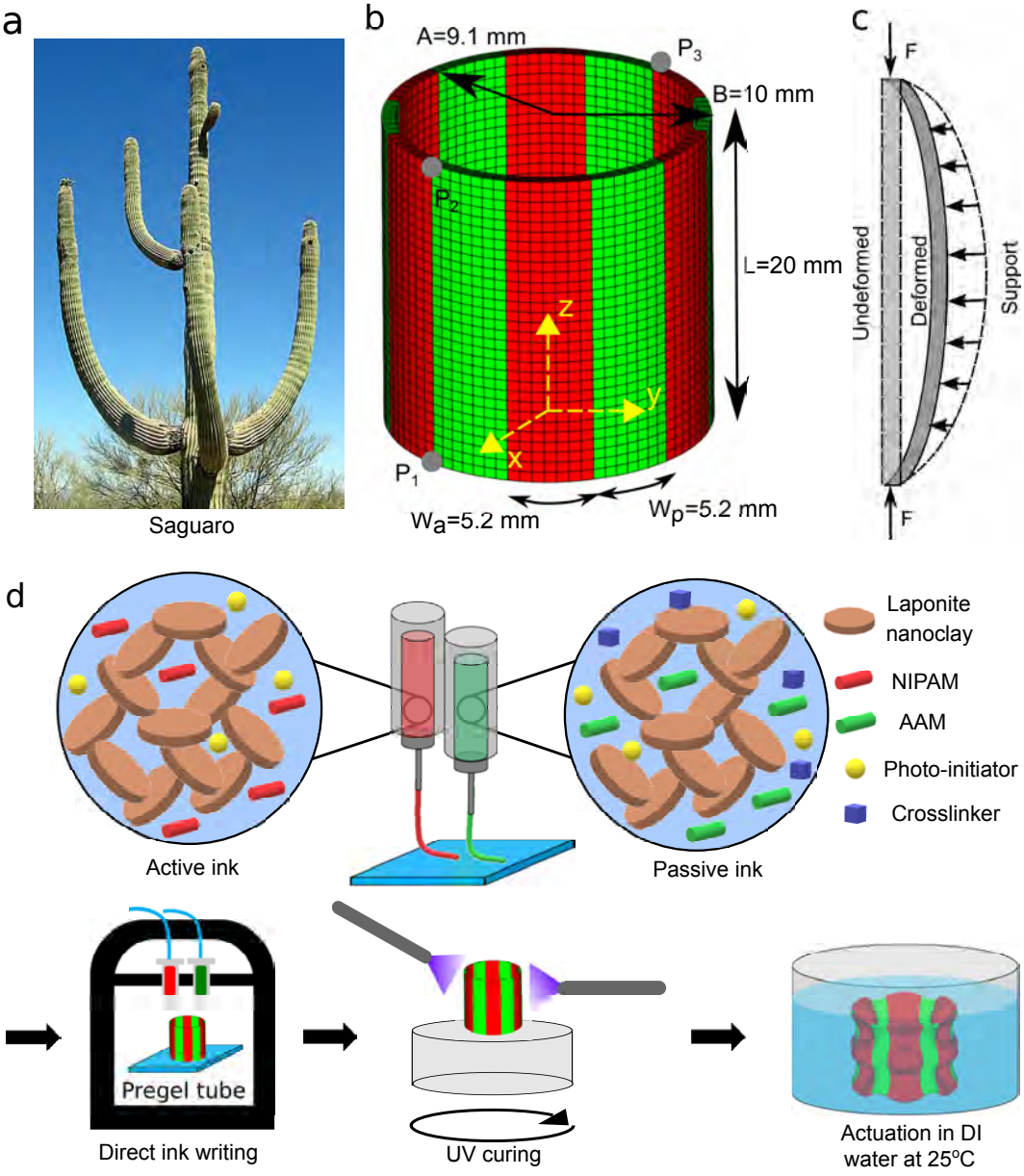

Figure 1: (a) A ribbed and buckled Saguaro stem in Arizona; printed with permission from Dave McShaffrey, Marietta College. (b) Finite element geometry of the baseline accordion structure with inner radius A, outer radius B, height L, active strip width W_a, and passive strip width W_p. Red represents the active pNIPAM hydrogel and green represents the passive pAAM hydrogel. (c) Schematic of buckling of a bar on an elastic foundation. (d) Schematic of materials synthesis and 4D printing process for the dual-gel accordion structure.

2.2. Finite element model

2.2.1. Finite element geometry

The finite element geometry was developed using the dimensions measured from the tubes after photocuring (Fig. 1b). The baseline model was a $L = 20$ mm long tube composed of alternating vertical active segments of width of W_a= 5.2 mm and passive segments of width of W_p= 5.2 mm. The inner and outer radii of the tube were A= 9.1 mm and B= 10 mm, respectively. The mesh was discretized using trilinear hexahedral brick elements of height 0.6 mm, width 0.7 mm and thickness 0.18 mm. The following boundary conditions were applied on three points located on the outer rim of the tube's top and bottom surfaces to prevent rigid body motion: $u_x = u_y = u_z = 0$ at $x = B$, $y = 0$, $z = 0$ (P_1); $u_x = u_y = 0$ at $x = B$, $y = 0$, $z = L$ (P_2), and $u_y = 0$ at $x = -B$, $y = 0$, $z = L$ (P_3).

2.2.2. Material model

The material behavior of the pAAM segments was described by a quasi-incompressible Neo-Hookean model (Eq. (1)). The shear modulus of the pAAM gel, $G = 11.9$ kPa, was measured using a dynamic mechanical analyzer (DMA Q800, TA instruments). Samples with a shape of a square disk were 3D printed using the process described in the previous section. We ensured that the samples reached equilibrium swelling by immersing them in DI water at the room temperature for at least 24 hrs. The samples were then measured at room temperature in air by uniaxial compression tests to a 2% applied strain. Stress-strain curves were generated from the raw static force and displacement data. The elastic modulus E was calculated as the tangent to the linear fit of stress-strain data, and the shear modulus G was calculated as $\frac{1}{3}E$ assuming mechanical incompressibility. The bulk modulus K of the pAAM gel was set to 1000 times of the shear modulus to achieve the nearly incompressible response, which is a commonly used assumption for modeling polymeric hydrogel materials. Equilibrium swelling tests of printed pAAM hydrogel tubes in DI water at different temperatures confirmed that the pAAM does not swell in response to a temperature change, which validates the choice of the hyperelastic Neo-Hookean model for pAAM.

The behavior of the pNIPAM segments was described by a coupled chemo-mechanical model developed previously for the thermoresponsive behavior of hydrogels and described in detail in [24, 25, 26]. The model can accurately predict the equilibrium configuration of pNIPAM gels and composite structures in response to different temperature and mechanical stimuli. The limitation of the model is that we neglected the kinetics of diffusion and could not capture the process of shape change at a given temperature. Briefly, the free energy of the hydrogel $\Psi = \Psi_e(\mathbf{F}, \phi) + \Psi_m(\phi)$ was assumed to be composed additively of a mechanical part Ψ_e for the stretching of polymer network and a chemical part Ψ_m for the mixing of the polymer network and solvent, where $\mathbf{F}$ is the deformation gradient tensor and ϕ is the polymer volume fraction of the hydrogel at the final deformed swollen state. We used a quasi-incompressible Neo-Hookean model to describe the strain energy density of the polymer network,

$$\Psi_e(\mathbf{F}, \phi) = \frac{G}{2}[\lambda_1^2 + \lambda_2^2 + \lambda_3^2 - 3 - 2\ln(\lambda_1\lambda_2\lambda_3)] + \frac{K}{4}[(\phi\lambda_1\lambda_2\lambda_3)^2 - 2\ln(\phi\lambda_1\lambda_2\lambda_3) - 1] \quad (1)$$

where G and K are the shear modulus and bulk modulus of the polymer network, and λ_1, λ_2, and λ_3 are the principal stretches of the deformation gradient tensor. The bulk modulus was assumed to be 1000 times of the shear modulus to achieve near mechanical incompressibility ($J_e = \phi\lambda_1\lambda_2\lambda_3 \simeq 1$).

The Flory-Huggins model was used to describe the free energy density of mixing [27],

$$\Psi_m(\phi) = \frac{RT}{v\phi}[(1-\phi)\ln(1-\phi) + \chi\phi(1-\phi)] \tag{2}$$

where R is the gas constant, T is the temperature, v is the volume per solute molecule, and χ is the Flory-Huggins interaction parameter. To model the thermoresponsive swelling of hydrogel, we assumed that the Flory-Huggins parameter depended on the temperature as follows [28],

$$\chi = \frac{1}{2}(\chi_L + \chi_H) + \frac{1}{2}(\chi_H - \chi_L)\tanh(\frac{T - T_{tran}}{\Delta T}) \tag{3}$$

where χ_L and χ_H are the Flory-Huggins parameters at low and high temperatures, T_{tran} is the LCST temperature, and ΔT is the width of temperature transition region. From the free energy density of the hydrogel, the Cauchy stress tensor of the hydrogel σ can be calculated from hyperelasticity theory, and the chemical potential of the hydrogel μ can be derived from the thermodynamics argument,

$$\sigma = \frac{1}{\det(\mathbf{F})}\frac{\partial\Psi}{\partial\mathbf{F}}\mathbf{F}^T \tag{4}$$

$$\mu = \frac{\partial\Psi}{\partial c} \tag{5}$$

where c is the number of solute molecules per polymer volume in the final deformed swollen state, and is related to ϕ through $\phi = \frac{1}{1+vc}$. The constitutive model was implemented in Tahoe (Sandia National Laboratories) for the finite element simulations of the hydrogel tubular structures.

To determine the model parameters for the pNIPAM gel, we applied standard dynamic mechanical analysis tests (DMA Q800, TA instruments) to measure the shear modulus G of 3D printed gel samples. Square disk shaped pNIPAM gel samples were 3D printed and allowed to swell in DI water at the room temperature for 24 hrs. Uniaxial compression tests were conducted on the printed gel samples in the same manner as described above for the pAAM gel samples. The Flory-Huggins interaction parameters χ_L, χ_H, T_{tran}, and ΔT were obtained by fitting the results of the equilibrium swelling tests of the printed gels at different temperatures (between 25°C and 50°C). For the equilibrium swelling tests, circular tubes of pNIPAM gel were 3D printed and photocured.The photos of the printed pNIPAM tubes were taken in a dark room using a digital camera (EOS 70D, Canon) and a broad spectrum UV light source (EF-160C, Spectronics) after photocuring and after immersed in DI water at the test temperature for 24 hours. The diameters of the printed pNIPAM tubes were measured manually using ImageJ software, and the volumetric change ratios of the pNIPAM gel at each test temperature compared with the photocured state were calculated. A small volumetric change ratio of 0.94 was obtained at the highest temperature 50°C. The equilibrium volumetric change ratio increased

to 1.33, 2.05, and 2.6 as the temperature was decreased to 41°C, 33°C and 25°C, respectively[5]. The material model parameters for the printed pNIPAM and pAAM gels are summarized in Table 1.

The simulation was started from the high temperature $T = 50°C$ to approximate the un-swollen photocured state. The initial polymer volume fraction ϕ_0 at this reference state was determined by solving the mechanical and chemical equilibrium equations (4)-(5). The swelling induced shape-change was simulated by linearly decreasing the temperature from 50°C to the room temperature 25°C and solving the mechanical and chemical equilibrium equations at each step.

	$G(kPa)$	χ_L	χ_H	$T_{tran}(^oC)$	$\Delta T(^oC)$
3D Printed pNIPAM	2.32	0.5	0.9	34	4
3D Printed pAAM	11.9	-	-	-	-

Table 1: The constitutive model parameters for 3D Printed pNIPAM and pAAM hydrogels

2.2.3. Parameter study

A parameter study was performed to investigate the effects of material properties and geometrical factors on the periodic buckling mode of the 4D printed hydrogel tubes. The five geometrical properties of the tube structure A, B, L, W_p, and W_a were combined into four dimensionless structural parameters: $\frac{B}{L}$, which describes the slenderness ratio, the diameter ratio $\frac{B}{A}$, the segment width ratio $\frac{W_p}{W_a}$, and $\frac{B}{W_p+W_a}$, which describes the number of alternating passive and active segments. The material behavior was described by two additional dimensionless parameters, the ratio of the Young's modulus of the passive and active segments $\frac{E_p}{E_a}$ and the volumetric swelling ratio $\Delta\theta$ of the pNIPAM hydrogel.

The six dimensionless parameters in the study were varied one-by-one over a wide range to evaluate the individual effects of the geometric and material factors (Table 2). The baseline values $\frac{E_p}{E_a} = 5$ and $\Delta\theta = 2.6$ were obtained from the experimental measurements as described in the prior section. Specifically, the ratio of $\frac{B}{L}$ (Table 2(a)), was varied by varying L to keep all other parameters constant. The diameter ratio and modulus ratio were changed by varying the parameter A and E_p respectively to keep all other parameters unchanged. The segment width ratio was varied by changing W_p and setting $W_a = \frac{2\pi B}{n} - W_p$, where $n = 6$ is the number of segments, to maintain all other parameters constant. The $\frac{B}{W_p+W_a} = \frac{n}{2\pi}$ was varied by changing the number of alternating passive and active segments from $n = 6$ to $n = 15$, while all other parameters were kept unchanged. The number of alternating segments were chosen based on the number of ribs on saguaro cacti (6 - 20) [4].

2.3. Buckling of bar sitting on an elastic foundation

Swelling of the pNIPAMs strips against the constraints of the adjacent elastic passive strips causes compressive stresses to develop in the swelling strips that are released by the buckling of the strip into a sinusoidal shape. The constrained swelling of a pNIPAM strip can be approximated as a beam supported by equally spaced elastic supports,

	$\frac{B}{L}$	$\frac{B}{A}$	$\frac{W_p}{W_a}$	$\frac{B}{W_p+W_a}$	$\frac{E_p}{E_a}$	$\Delta\theta$
(a)	$0.2-1$	1.1	1	$\frac{6}{2\pi}$	5	2.6
(b)	0.5	$1.04-1.5$	1	$\frac{6}{2\pi}$	5	2.6
(c)	1	1.1	$0.25-5$	$\frac{6}{2\pi}$	5	2.6
(d)	0.5	1.1	1	$\frac{6}{2\pi}-\frac{15}{2\pi}$	5	2.6
(e)	0.5	1.1	1	$\frac{6}{2\pi}$	$5-250$	2.6
(f)	0.5	1.1	1	$\frac{6}{2\pi}$	5	$2.6-24$

Table 2: The simulation design parameters for the parameter study

subjected to a compressive load in the axial direction (Fig. 1c). Timoshenko and Gere [29] provide a detailed theoretical analysis for the buckling of this structure. The concentrated axial force of the beam on the elastic foundation is given by:

$$F = \frac{\pi^2 EI}{l^2}(m^2 + \frac{\beta l^4}{m^2\pi^4 EI}) \tag{6}$$

where E, I, and l represent the Young's modulus, second moment of inertia, and length of the bar, β is the Young's modulus of the elastic foundation, and m is the number of half sine waves of the buckling mode. The number of half sine waves (m) is calculated by minimizing the critical load F in Eq. (6) with respect to m. Thus the number of half sine waves at buckling of the bar depends on the geometry dimension of the bar, and the elastic moduli of the bar and the foundation. Considering the special case when $\beta = 0$, there is no elastic foundation and minimizing Eq. (6) gives $m = 1$. For flexible foundation (β is very small), m is constant at 1 meaning that the bar buckles without an intermediate inflection point. By gradually increasing the elastic modulus of the foundation β, we can reach a situation where $m = 3$ gives a smaller F than $m = 1$. Setting F to be at the same at m and $m+2$ gives the following buckling coefficient of the bar, which signifies the ratio of the structural stiffness of the foundation and bar, at the transition between two buckling modes,

$$\omega_{bar} = \frac{\beta l^4}{\pi^4 EI} = m^2(m+2)^2 \tag{7}$$

Equation (7) can be used to determine the buckling mode, characterized by m, for given a dimension of the bar and elastic moduli of the bar and the foundation. For values of ω_{bar} smaller than $m^2(m+2)^2$, the deflection curve of the buckled bar has m half sine waves; for ω_{bar} larger than $m^2(m+2)^2$, the bar will be buckled into $m+2$ half sine waves (Table 3).

For the vertical segments in the tube of length L, width $w = \frac{\pi B}{6}$ and thickness $h = B - A$, $E = E_a$ and $\beta = E_p$, the second moment of area can be approximated as $I = \frac{1}{12}wh^3 = \frac{\pi B}{72}(B-A)^3$ by neglecting the curvature of the segments. Then the buckling coefficient in Eq. (7) can be expressed as,

$$\omega_{tube} = C\frac{72E_pL^4}{\pi^5 E_a B(B-A)^3} \tag{8}$$

Buckling coefficient, ω_{bar}	Number of half sine waves at buckling, m
$\omega_{bar} \leq 9$	$m = 1$
$9 < \omega_{bar} \leq 225$	$m = 3$
$225 < \omega_{bar} \leq 1225$	$m = 5$
$1225 < \omega_{bar} \leq 3969$	$m = 7$
$3969 < \omega_{bar} \leq 9801$	$m = 9$

Table 3: The buckling coefficient and number of half sine waves for a bar on elastic foundation.

where C is a constant that accounts for the effects of finite deformation and of geometrical features not considered in the theoretical beam model. For example, the active segments in the tube were supported by adjacent elastic passive strips, while in the original theory the bar was sitting on the elastic foundation.

3. Results and discussions

We first simulated the equilibrium buckling deformation of the baseline 4D-printed tube observed in experiments (Fig. 2a). The swelling tests subjected the printed tube immersed in DI water to stepwise temperature changes from 50°C to 25°C. The temperature was held constant for 24 hrs to achieve the equilibrium swelling shape. In the simulations, the temperature was decreased continuously from 50°C to 25°C, and the equilibrium shape was evaluated at each temperature by solving Eq. (4)-(5) for mechanical and chemical equilibrium. The constrained swelling of pNIPAM strips during cooling caused compressive axial stresses to build up in the pNIPAM strips (Fig. 2b) until periodic buckling of mode $m = 3$ was initiated at 36°C. Buckling allowed the compressive axial stresses to be relieved by the lateral deflection of the strip into a full sine wave characteristic of mode 3 buckling. The amplitude of the buckling mode increased with decreasing temperature, which results in an increase in the maximum diameter of the swollen tube by 53% at 25°C (Fig. 2c), which agreed quantitatively with experimental measurements of the diameter ratio $\frac{B_{swollen}}{B_{initial}}$ in the equilibrium swelling tests (Fig. 2a).

We next investigated the effect of the material and geometric factors on the buckling mode of the 4D-printed tube. Decreasing $\frac{B}{L}$ from 1 to 0.2 caused the tubes to become more slender and more susceptible to higher buckling modes. The number of half sine waves predicted by the finite element simulations increased from 1 to 9 (Fig. 3a). Decreasing $\frac{B}{A}$ reduced the thickness of the tube, which decreased flexural stiffness and caused the tubes to experience higher buckling modes (Fig. 3b). Varying the ratio of the segment widths $\frac{W_p}{W_a}$ from 0.25 to 5 changed the amplitude of the buckling mode but did not induce a higher bucking mode (Fig. 3c). We calculated the axial force f on the passive segments exerted by the active segments, by integrating the normal axial stress σ_{zz} on the $z = \frac{L}{2}$ plane surface of the passive segments at 25°C. The axial load on the passive segments was defined by dividing f with passive segment width W_p. When the segment width ratio $\frac{W_p}{W_a}$ increased from 0.25 to 5, the axial load $\frac{f}{W_p}$ decreased by 81%, and the

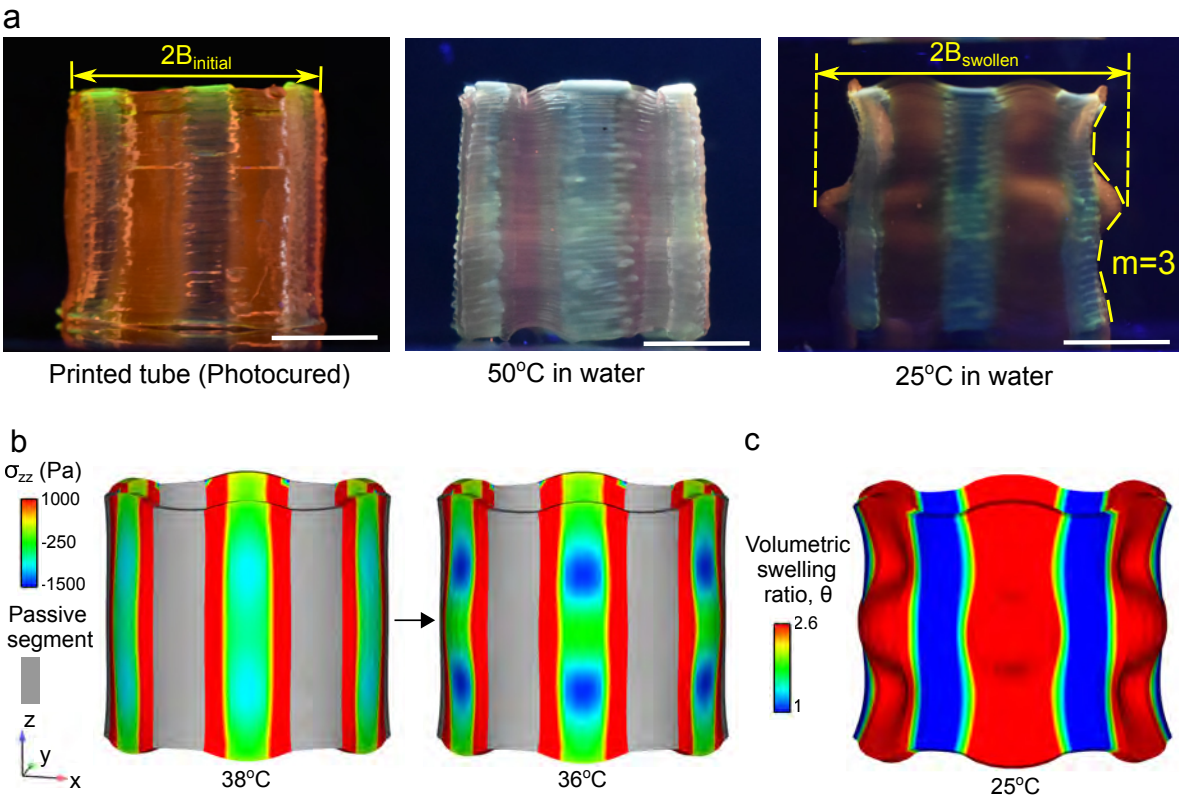

Figure 2: (a) Experimental pictures of the actuation tests of the printed baseline accordion structure. $2B_{initial}$ and $2B_{swollen}$ represent the outer diameter of the tube in the initial unswollen state and swollen state at 25°C, respectively. Scale bar indicates 1 cm. (b) Contour plots of the axial stress (σ_{zz}) developed in the active segments until the initiation of buckling at 36°C for the simulated baseline accordion model. (c) Contour plot of the pNIPAM volumetric swelling ratio θ for the simulated equilibrium shape at 25°C.

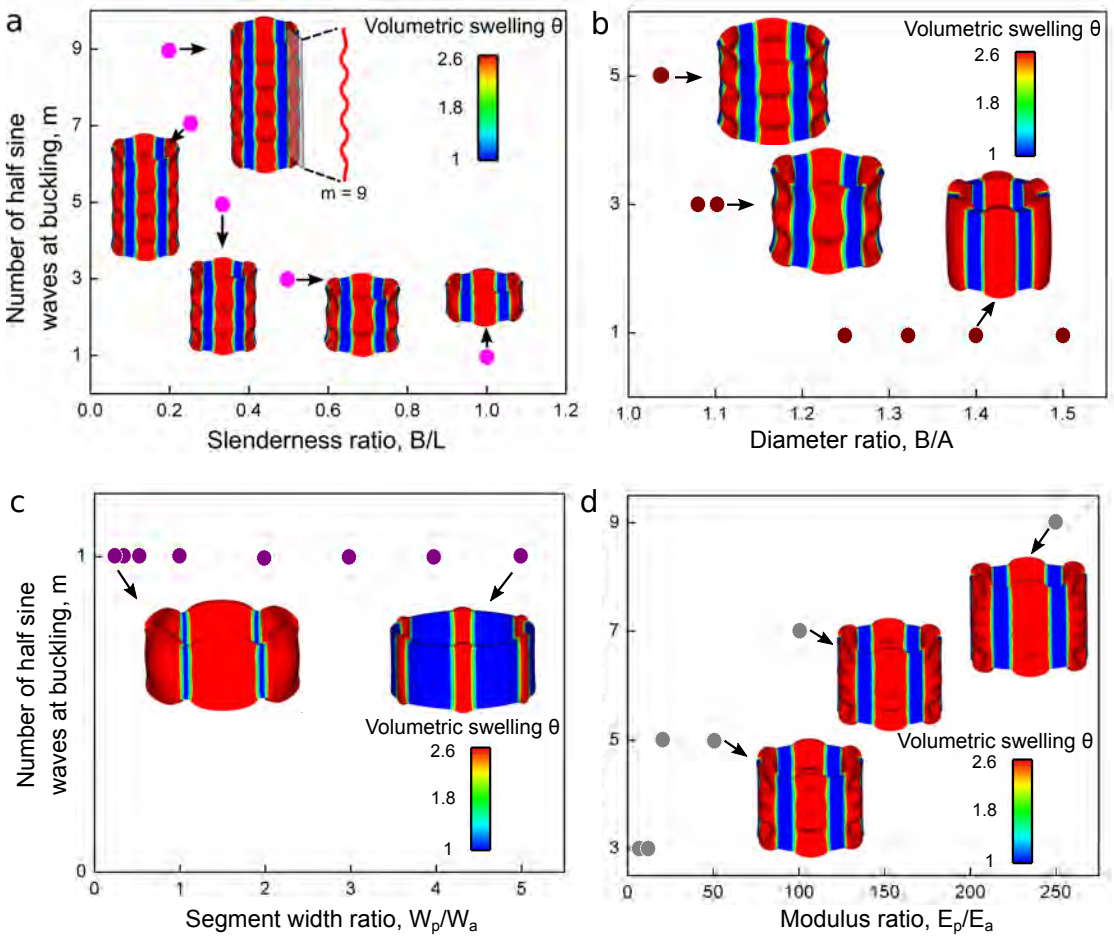

Figure 3: The effects of dimensionless material and geometric parameters on the periodic buckling modes: (a) slenderness ratio $\frac{B}{L}$ (pink), (b) diameter ratio $\frac{B}{A}$ (maroon), (c) segment width ratio $\frac{W_p}{W_a}$ (purple), and (d) modulus ratio $\frac{E_p}{E_a}$ (grey). The parameters were varied one by one in the parameter study. Contour plots of the volumetric swelling ratio θ of the hydrogel in the swollen configuration at 25°C are included in the inset.

narrow pNIPAM strips could not exert enough force to buckle the whole tube structure. As a result, the diameter change from the unswollen to the swollen buckled state decreased by 71%. Increasing the number of alternating segments $\frac{B}{W_p+W_a}$ did not affect the buckling mode, but increased the swelling ratio of active segments needed to initiate buckling. From finite element simulations, we found that for tubes with $n = 6, 9, 12, 15$ alternating active and passive segments, the volumetric swelling ratio $\Delta\theta$ needed for the initiation of buckling were 1.9, 2.9, 6.1, and 10.9 respectively.

Increasing the modulus ratio E_p/E_a had a similar effect to decreasing the slenderness ratio and diameter ratio. Increasing the modulus of the passive pAAM strips produced a higher compressive loading on the pNIPAM strips resulting in higher buckling mode with a larger number of half sine waves at buckling (Fig. 3d). The elastic modulus of the hydrogel layers can be made larger through higher shear-thinning agent concentration, higher polymer concentration, or higher crosslinking density. As expected, varying the swelling ratio $\Delta\theta$ of pNIPAM had the same effect as

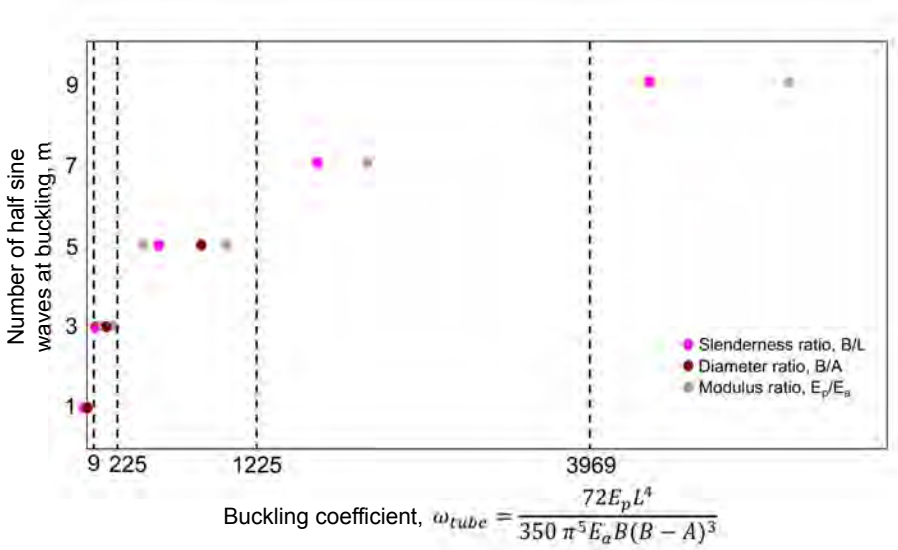

Figure 4: Phase diagram for the periodic buckling modes of tubes with different structural geometries and material properties. Pink, maroon, and grey dots represent the simulation results in the parameter study when varying the slenderness ratio $\frac{B}{L}$, diameter ratio $\frac{B}{A}$, and modulus ratio $\frac{E_p}{E_a}$ one at a time. The transitions between the buckling mode (–) occurs at $\omega_{tube} = m^2(m+2)^2$.

varying the temperature. Increasing $\Delta\theta$ from 2.6 to 24 caused the diameter swelling ratio to increase by 78%, but did not affect the buckling mode.

The finite element modeling study showed that the number of half sine waves of the buckled accordion can be tuned by varying $\frac{B}{L}$, $\frac{B}{A}$, and $\frac{E_p}{E_a}$. Changing the segment width ratio $\frac{W_p}{W_a}$, number of segments $\frac{B}{W_p+W_a}$, and volumetric swelling ratio $\Delta\theta$ did not alter the buckling mode. The fitting parameter $C = \frac{1}{350}$ of the critical buckling coefficient for the tubes in Eq. (8) was determined to satisfy $\omega_{tube} = m^2(m+2)^2$ for the cases of the parameter study (Fig. 4). The resulting $\omega_{tube} = \frac{72E_pL^4}{350\pi^5 E_a B(B-A)^3}$ provides a design parameter for the periodic folding of the composite tube that combines the effects of geometry and material properties of the active and passive segments.

The modeling outcomes were validated by 3D printing three selected cases from the parameter study and performing the swelling experiments in DI water at the room temperature (Fig. 5). The three cases were: $\frac{B}{L} = 0.5$, $\frac{B}{A} = 1.04$, and $\frac{E_p}{E_a} = 5$ (Fig. 5a); $\frac{B}{L} = 0.33$, $\frac{B}{A} = 1.1$, and $\frac{E_p}{E_a} = 5$ (Fig. 5b); and $\frac{B}{L} = 0.25$, $\frac{B}{A} = 1.1$, and $\frac{E_p}{E_a} = 5$ (Fig. 5c). The printed tubes were immersed in DI water for 24 hours and the deformed configuration showed the same buckling mode with the same number m of half sine waves as predicted by the FEA simulations and the critical buckling coefficient ω_{tube}. The experiment was repeated 2-3 times for each case with the same result.

4. Conclusions

We designed stimuli responsive periodic buckling tubes composed of alternating soft active segments and stiff passive segments. We investigated the buckling modes of the tube using a combination of theoretical and finite ele-

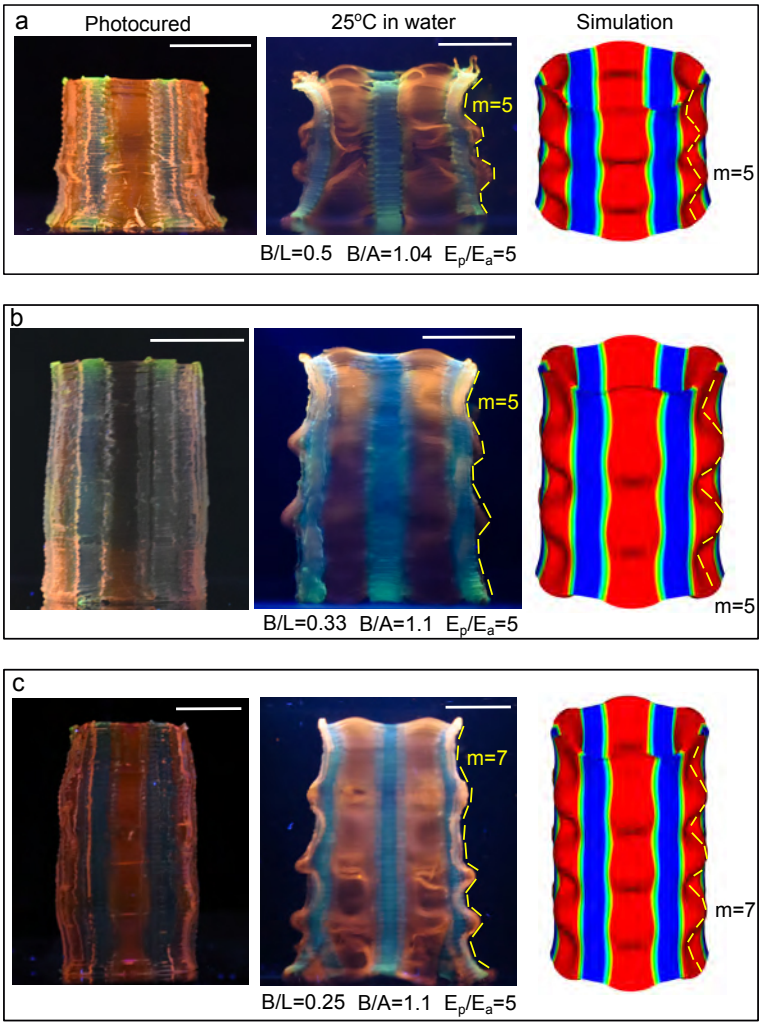

Figure 5: Images from the photocured and the actuated tubes exhibiting different periodic buckling modes along with simulation snapshots. Tubes with different design parameters were printed: (a) $\frac{B}{L} = 0.5$, $\frac{B}{A} = 1.04$, and $\frac{E_p}{E_a} = 5$; (b) $\frac{B}{L} = 0.33$, $\frac{B}{A} = 1.1$, and $\frac{E_p}{E_a} = 5$; and (c) $\frac{B}{L} = 0.25$, $\frac{B}{A} = 1.1$, and $\frac{E_p}{E_a} = 5$. In the experimental pictures, the active pNIPAM and passive pAAM hydrogels show fluorescent orange and green colors, and the scale bar indicates 1 cm. In the simulation snapshots, the contour plots of the volumetric swelling ratio θ of the hydrogel are shown for the deformed equilibrium configuration at 25°C.

ment modeling and verified the buckling modes with 4D printing experiments. The model included six dimensionless design parameters that describe the geometry and material properties of the active and passive segments. From the simulations, we observed that the number of half sine waves at buckling varied with three design parameters individually: slenderness ratio $\frac{B}{L}$, diameter ratio $\frac{B}{A}$, and modulus ratio $\frac{E_p}{E_a}$. The other three design parameters, segment width ratio $\frac{W_p}{W_a}$, number of alternating segments $\frac{B}{W_p+W_a}$, and volumetric swelling ratio $\Delta\theta$, did not affect the buckling modes. Approximating the buckled segment as the buckling of a bar on an elastic foundation, we developed a universal design parameter, ω_{tube}, that combines the effects of geometry dimensions, modulus and swelling ratio, and constructed a phase diagram of the periodic buckling modes of the tubes, that were validated by experiments. The design parameter provides an efficient rule for the design of self-morphing tubes that can expand radially with negligible axial elongation that have potential applications to deployable and morphing biomedical implantable devices and actuators for soft robotics. The combined theoretical and computational approach represents a powerful framework to develop analytical design parameters for tailoring buckling instabilities of active hydrogel structures.

Acknowledgement

We acknowledge funding from the National Science Foundation EFMA-1830893 and DMR-1709349.

Declarations of interest

None.

References

[1] W. Barthlott, M. Mail, B. Bhushan, K. Koch, Plant surfaces: structures and functions for biomimetic innovations, Nano-Micro Letters 9 (2) (2017) 23.

[2] P. S. Nobel, Surface temperatures of cacti–influences of environmental and morphological factors, Ecology 59 (5) (1978) 986–995.

[3] K. J. Niklas, S. L. Buchman, The allometry of saguaro height, American Journal of Botany 81 (9) (1994) 1161–1168.

[4] A. Altesor, E. Ezcurra, Functional morphology and evolution of stem succulence in cacti, Journal of arid environments 53 (4) (2003) 557–567.

[5] J. Liu, O. Erol, A. Pantula, W. Liu, Z. Jiang, K. Kobayashi, D. Chatterjee, N. Hibino, L. H. Romer, S. H. Kang, et al., Dual-gel 4d printing of bioinspired tubes, ACS applied materials & interfaces.

[6] Y. Hirokawa, T. Tanaka, Volume phase transition in a non-ionic gel, in: AIP Conference Proceedings, Vol. 107, Aip, 1984, pp. 203–208.

[7] C. Y. Li, X. P. Hao, Z. L. Wu, Q. Zheng, Photolithographically patterned hydrogels with programmed deformations, Chemistry–An Asian Journal 14 (1) (2019) 94–104.

[8] Z. Liu, S. Swaddiwudhipong, W. Hong, Pattern formation in plants via instability theory of hydrogels, Soft Matter 9 (2) (2013) 577–587.

[9] J. Yin, Z. Cao, C. Li, I. Sheinman, X. Chen, Stress-driven buckling patterns in spheroidal core/shell structures, Proceedings of the National Academy of Sciences 105 (49) (2008) 19132–19135.

[10] J. Yin, X. Chen, I. Sheinman, Anisotropic buckling patterns in spheroidal film/substrate systems and their implications in some natural and biological systems, Journal of the Mechanics and Physics of Solids 57 (9) (2009) 1470–1484.

[11] P. D. Shipman, A. C. Newell, Phyllotactic patterns on plants, Physical review letters 92 (16) (2004) 168102.

[12] P. Shipman, A. C. Newell, Polygonal planforms and phyllotaxis on plants, Journal of theoretical biology 236 (2) (2005) 154–197.

[13] A. C. Newell, P. D. Shipman, Plants and fibonacci, Journal of Statistical Physics 121 (5-6) (2005) 937–968.

[14] P. B. Green, C. Steele, S. Rennich, Phyllotactic patterns: a biophysical mechanism for their origin, Annals of Botany 77 (5) (1996) 515–528.

[15] C. R. Steele, Shell stability related to pattern formation in plants, Journal of Applied Mechanics 67 (2) (2000) 237–247.

[16] J. Dervaux, P. Ciarletta, M. B. Amar, Morphogenesis of thin hyperelastic plates: a constitutive theory of biological growth in the föppl–von kármán limit, Journal of the Mechanics and Physics of Solids 57 (3) (2009) 458–471.

[17] M. B. Amar, P. Ciarletta, Swelling instability of surface-attached gels as a model of soft tissue growth under geometric constraints, Journal of the Mechanics and Physics of Solids 58 (7) (2010) 935–954.

[18] Y. Forterre, J. M. Skotheim, J. Dumais, L. Mahadevan, How the venus flytrap snaps, Nature 433 (7024) (2005) 421.

[19] H. Liang, L. Mahadevan, The shape of a long leaf, Proceedings of the National Academy of Sciences 106 (52) (2009) 22049–22054.

[20] S. J. Gerbode, J. R. Puzey, A. G. McCormick, L. Mahadevan, How the cucumber tendril coils and overwinds, Science 337 (6098) (2012) 1087–1091.

[21] Y. Yang, H.-H. Dai, F. Xu, M. Potier-Ferry, Pattern transitions in a soft cylindrical shell, Physical review letters 120 (21) (2018) 215503.

[22] L. Stein-Montalvo, P. Costa, M. Pezzulla, D. P. Holmes, Buckling of geometrically confined shells, Soft matter 15 (6) (2019) 1215–1222.

[23] O. Erol, A. Pantula, W. Liu, D. H. Gracias, Transformer hydrogels: A review, Advanced Materials Technologies (2019) 1900043.

[24] J. Guo, T. Shroff, C. Yoon, J. Liu, J. C. Breger, D. H. Gracias, T. D. Nguyen, Bidirectional and biaxial curving of thermoresponsive bilayer plates with soft and stiff segments, Extreme Mechanics Letters 16 (2017) 6–12.

[25] J. C. Breger, C. Yoon, R. Xiao, H. R. Kwag, M. O. Wang, J. P. Fisher, T. D. Nguyen, D. H. Gracias, Self-folding thermo-magnetically responsive soft microgrippers, ACS applied materials & interfaces 7 (5) (2015) 3398–3405.

[26] C. Yoon, R. Xiao, J. Park, J. Cha, T. D. Nguyen, D. H. Gracias, Functional stimuli responsive hydrogel devices by self-folding, Smart Materials and Structures 23 (9) (2014) 094008.

[27] P. J. Flory, J. Rehner Jr, Statistical mechanics of cross-linked polymer networks i. rubberlike elasticity, The journal of chemical physics 11 (11) (1943) 512–520.

[28] S. A. Chester, L. Anand, A thermo-mechanically coupled theory for fluid permeation in elastomeric materials: application to thermally responsive gels, Journal of the Mechanics and Physics of Solids 59 (10) (2011) 1978–2006.

[29] S. P. Timoshenko, J. M. Gere, Theory of elastic stability, Courier Corporation, 2009.